



## Beamforming for large-area scan and improved SNR in array-based photoacoustic microscopy

A. Cebrecos <sup>\*</sup>, J.J. García-Garrigós, A. Descals, N. Jiménez, J.M. Benlloch, F. Camarena

*Instituto de Instrumentación para Imagen Molecular (i3M), Consejo Superior de Investigaciones Científicas (CSIC), Universitat Politècnica de València (UPV), Camino de Vera s/n, 46022, Valencia, Spain*



### ARTICLE INFO

**Keywords:**

Photoacoustic imaging  
OR-PAM  
Array-based  
DAS beamforming  
Large-area scan  
Pulsed laser diode

### ABSTRACT

Beamforming enhances the performance of array-based photoacoustic microscopy (PAM) systems for large-area scan. In this study, we quantify the imaging performance of a large field-of-view optical-resolution photoacoustic-microscopy system using an phased-array detector. The system combines a low-cost pulsed-laser diode with a 128-element linear ultrasound probe. Signal-to-noise ratio (SNR) and generalized contrast-to-noise ratio (gCNR) are quantified using the phased-array detector and applying three beamforming strategies: a no-beamforming method equivalent to a single-element flat transducer, a fixed focus beamforming method that mimics a single-element focused transducer, and a dynamic focus beamforming using a delay-and-sum (DAS) algorithm. The imaging capabilities of the system are demonstrated generating high-resolution images of tissue-mimicking phantoms containing sub-millimetre ink tubes and an ex vivo rabbit's ear. The results show that dynamic focus DAS beamforming increases and homogenizes SNR along 1-cm<sup>2</sup> images, reaching values up to 15 dB compared to an unfocused detector and up to 30 dB compared to out-of-focus regions of the fixed focus configuration. Moreover, the obtained values of gCNR using the DAS beamformer indicate an excellent target visibility, both on phantoms and ex vivo. This strategy makes it possible to scan larger surfaces compared to standard configurations using single-element detectors, paving the way for advanced array-based PAM systems.

### 1. Introduction

Photoacoustic microscopy (PAM) is an imaging technique that combines optical excitation with ultrasound reception to form images from directly depth-resolved signals by raster-scanning the sample without applying reconstruction algorithms [1,2]. It has received a growing interest over the last decade for its ability to provide anatomical, molecular, and functional imaging. As a short laser pulse is aimed at superficial biological tissue, some of the photons are absorbed by chromophores (oxyhemoglobin, deoxyhemoglobin, etc.) or exogenous contrast agents, inducing a local and fast temperature rise. As a result of the local thermoelastic expansion a pressure rise is produced leading to the generation of ultrasonic waves, a phenomenon known as the photoacoustic effect [3].

PAM is typically classified in two main categories, optical-resolution (OR-PAM) [4], based on the optical ballistic regime, and acoustic resolution (AR-PAM) [5], based on the diffusive regime. In OR-PAM, the laser excitation is tightly focused and hence, the size of the laser spot determines the lateral resolution, at the expense of a shallow penetration as compared with AR-PAM [1].

For the light source, OR-PAM typically uses different types of short-pulsed solid state lasers, such as Nd:YLF [4], Nd:YAG [6], Nd:YVO4 [7], or even Ti:Sapphire [8]. They provide short pulses and high energy per pulse, although they generally have a high cost, large size and require a bulky cooling system. Moreover, the repetition rate may be relatively low [9]. As an inexpensive and more compact alternative, pulsed laser diodes (PLD) [10–15] or light emitting diodes (LED) [16–18] are often employed (see Ref. [19] for a thorough review on low-cost sources). Their main drawback is their poor signal-to-noise ratio (SNR) which usually requires multiple averaging.

Regarding ultrasound detectors, conventional OR-PAM systems rely on piezoelectric transducers or optical-acoustic detectors (such as Fabry-Perot ultrasound sensors) [20]. Many piezoelectric-based OR-PAM systems use single-element focused transducers with focal spots of very few mm<sup>2</sup>, limiting the field-of view (FOV) of the image. Commonly, to increase the FOV, the detector is mechanically displaced relative to the sample, but this requires the immersion of the detector in a fluid to grant acoustic coupling, increasing the complexity of the system. Conversely, fibre optic sensors with improved sensitivity and

\* Corresponding author.

E-mail address: [alcebrui@upv.es](mailto:alcebrui@upv.es) (A. Cebrecos).

wide acceptance of angles have been proposed as good candidates to increase the field-of-view (FOV) of photoacoustic images without the need for translational mechanical scanning [21,22].

While phased-arrays detectors are commonly used in other optoacoustic modalities such as photoacoustic tomography (PAT), they have not been exploited intensively in PAM. Initially, some existing array-based PAM systems were designed to improve the imaging speed in order to obtain real-time imaging systems [23–25]. Array-based OR-PAM systems have been used in microendoscopy to produce small images ( $<1 \text{ mm}^2$ ) by using a fibre laser and a 128-element ultrasound linear array [26]. It also has been explored the advantages of delay-and-sum (DAS) beamforming within the surface of an imaging plane of  $3 \times 1.5 \text{ mm}^2$  using a Q-switched Nd:YAG laser, showing that SNR improves when comparing 64-element phased-array images and images obtained using only one element of the phased array [27]. However, the full capabilities of DAS beamforming within the imaging plane to further increase the FOV using low-cost PLD excitations and enhance SNR and other indexes such as generalized contrast-to-noise ratio (gCNR) [28] with respect to flat or focused ultrasound detectors remains unexplored and has not been quantified to date.

In this work, we study the performance of DAS beamforming to improve image quality in large-area scans using an array-based OR-PAM system and a low-cost PLD excitation. Large area DAS beamformed images of  $12 \times 4 \text{ mm}^2$  and  $20 \times 2 \text{ mm}^2$  are compared with the ones obtained using fixed focus and unfocused detectors, and the SNR and gCNR is quantified. We show that DAS beamforming makes it possible to greatly increase and spatially homogenize the SNR of the image, especially in out-of-focus regions, as compared to OR-PAM using single-element detectors. In addition, the use of DAS beamforming avoids the need to displace the ultrasound probe with respect to the imaged sample. Images of sub-millimetre polyethylene tubes filled with India ink embedded in tissue mimicking phantoms and the microvasculature of an ex vivo rabbit ear were acquired in order to evaluate the performance of the system. A detailed laser beam spot characterization was performed by both optical and acoustical means yielding a lateral resolution of  $200 \times 119 \mu\text{m}^2$ , while the experimental results of the developed PAM system demonstrate a spatially homogenized SNR increase up to nearly 30 dB for out-of-focus regions along a large area scan of around  $1 \text{ cm}^2$ , compared to a classical fixed focus configuration, as well as very high gCNR values, demonstrating an excellent target visibility.

## 2. Materials and methods

### 2.1. Laser diode excitation and beam optics configuration

A high-power PLD of 650 W output peak power and  $905 \pm 10 \text{ nm}$  central wavelength was used (model 905D5S2L3J08X, Laser Components, Germany). As depicted in Fig. 1, the laser diode is driven by forward current pulses from a variable voltage driver module (LDP-V 80-100, PicoLAS, Germany) in order to produce a burst of optical power pulses at a 2 kHz repetition rate and 100 ns pulse width (0.02% duty cycle) during a given excitation time. The PLD pulsed operation was set to a safe and non-destructive regime well below its absolute maximum ratings of 150 ns pulse width and 0.1% duty cycle. The laser diode driver is first configured from a dedicated microcontroller-based board, which sets the laser diode output power, ranging linearly from the laser threshold up to the maximum optical for the driver voltages 23–100 V; and also monitors safe operation settings like temperature and voltage limits. Afterwards, it runs as a signal-follower of the square pulse train sent by the pulse generator to the driver input signal port. Timing synchronization between the ultrasound DAQ system and PLD output pulses is achieved through a TTL trigger signal generated by the ultrasound system to the pulse generator.

The PLD is a mini-stack of 30 single-emitters arranged in 2 columns with 5 bars of 3 emitters each, which results in a structured light

pattern emitted from a whole rectangular area of  $800 \times 440 \mu\text{m}^2$ . It emits an elliptic and relatively high divergent beam with full-angle divergence of  $10^\circ$  and  $25^\circ$  for the horizontal (slow axis) and vertical (fast axis) planes, respectively. The PLD beam quality for each plane is  $M^2 \approx (121, 166)$ , which can be determined from the well-known relation  $BPP = M^2(\lambda/\pi)$  for its nominal wavelength  $\lambda = 905 \text{ nm}$  and  $BPP \approx (35, 48) \text{ mm mrad}$ , the beam-parameter product of the emitting surface radius and half-divergence,  $BPP \equiv w_0 \theta$ . Laser diode stacks have in general high M-squared values, much greater than a diffraction-limited beam  $M^2 \gg 1$  due to their inherently multimodal emission, which will limit the smallest beam spot size achievable by any optics, and ultimately the lateral resolution of OR-PAM imaging systems.

The optics scheme used to deliver and concentrate the laser beam power from the PLD into a small spot excitation area inside the imaging target (phantom or tissue) is shown in Fig. 1. The PLD optics comprises two planoconvex aspheric lenses, both with suitable anti-reflection coatings in the NIR range. A first lens of  $f_1 = 20.1 \text{ mm}$  focal length, a diameter of 25 mm and high numerical aperture NA=0.6 (ACL2520U-B, Thorlabs), is used to collect and collimate, or pre-focus, the light from a highly divergent beam emitted by the PLD stack. A second lens of shorter focal length of  $f_2 = 10.5 \text{ mm}$ , with 12 mm on diameter and NA=0.54 (ACL1210U-B, Thorlabs), focalizes the laser into a small spot area corresponding to the beam waist at the focus of this two-lens optical scheme. The aperture stop of this configuration is limited to the clear aperture of the focusing lens CA=10.8 mm. The distances for this optical configuration were set to:  $s_1 = 50 \text{ mm}$  from the laser diode emitting surface to the collimating lens object principal plane  $H_1$ , and  $s_2 = 11 \text{ mm}$  from there to the focusing lens image principal plane  $H'_2$ . The working distance (WD) is defined from the last lens mount surface to the focused beam waist giving thus the useable laser excitation depth inside the target volume, as depicted in the optical schematic of Fig. 1. After simulations of this optical configuration, based on both ray-tracing (Zemax, USA) and M-squared-corrected Gaussian optics (ReZonator, Chunosov, Russia), the WD for our setup was set to 2.3 mm on air, and 3 mm on water (with refractive index  $n = 1.33$ ). Note that the WD from the lens backplane would be longer but it is shortened by the lens mount fixing ring of 1.7 mm width.

The laser power distribution cross-section at the beam focus was first obtained from ray-tracing simulation and imaged by a camera in order to better determine the beam spot size and also the power eventually delivered to it, as presented later in Section 3.1. The beam spot image was taken with a beam profiler CCD camera (LT665, Ophir, Israel) and a lens of  $f = 60 \text{ mm}$  focal length placed in the optical axis at  $4f$  and  $2f$  distances respectively (1:1 magnification). The beam spot size given by optical means can then be compared to the beam spot size measured from the photoacoustic images, applying the Edge Spread Function (ESF) method, as a way of cross-checking and validate both imaging measurements.

The laser power measurements were performed with a calibrated integrating sphere (AvaSphere-30) with a 6 mm diameter input port aperture, connected by a optical fibre (FC-UVIR600-1-ME) to a Czerny-Turner monochromator spectrometer (AvaSpec-ULS2048XL-EVO) with 1.5 nm spectral resolution, being all these elements from Avantes, Netherlands. The beam power was measured with the integrating sphere placed in two different locations collecting all the light through its input port opening. One in front of the PLD to get 510 W of total emitted power (according to PLD specifications for the maximum driver current of 45 A and 100 V); and the second, just after the focusing optics with the integrating sphere opening at the beam focal plane, getting there a PLD power delivery of 300.5 W (which yields a power transport efficiency of 59% for the optics setup described before). The last measurement was then used in the optical simulation to calibrate the power distribution image at the same focal plane, so that the power delivered into a delimited spot area can be estimated more accurately, as detailed in Section 3.1. Both power measurements were analysed in the spectrometer by averaging 1000 laser pulses acquired for a 10 ms time integration window per pulse, and after integrating the full spectrum, with measured central wavelength and bandwidth of  $907 \pm 7 \text{ nm}$  in agreement with the PLD specifications.

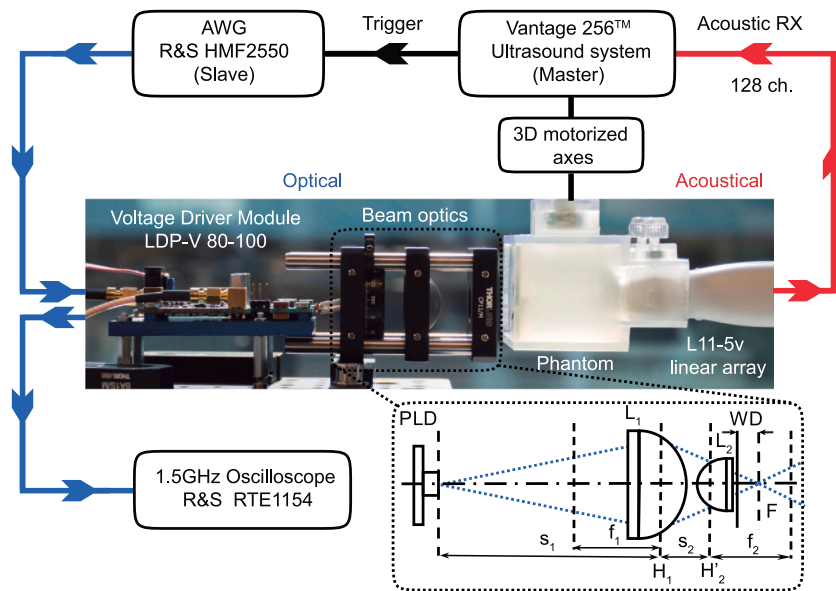


**Fig. 1.** Schematic diagram and main building blocks of the PAM system. Blue arrows refer to the signals of the optical part, starting from the arbitrary waveform generator to the driver and oscilloscope, while red lines represent the received acoustic signals from the ultrasound probe to the Vantage system, which acts as the master and controls trigger, emitted and received signals, as well as the mechanical rastering of the sample. A detailed beam optic diagram is included describing the PLD optical configuration for focusing the laser beam at the focusing plane (F).

## 2.2. Phantom preparation

Gelatin-based phantoms were produced inside a custom-made plastic container using 6% m/V of gelatin 200–220 bloom, adding 0.1% m/V of formaldehyde to increase long-term stability [29]. Hollow polyethylene tubes (0.85 mm out-diameter, 0.42 mm in-diameter) filled with India ink were inserted close to the surface of the gelatin to simulate blood vessels. The phantom container was attached to a 3D scanning motor for positioning and raster-scanning of the sample in a two-dimensional plane perpendicular to the laser beam at its focusing plane.

## 2.3. Ultrasound detection and beamforming

As illustrated in Fig. 1, the system uses a transmission mode configuration where the incident light and the US reception are located at opposite sides of the sample. The ultrasound acquisition system is a Vantage 256™ (Verasonics, USA) connected to a 128-element linear US probe (L11-5v, Verasonics, USA). The Vantage system generates the TTL trigger signal that synchronizes the arbitrary waveform generator that sends the electrical pulses to the Voltage Driver Module and PLD. Acoustic signals are collected across all 128 elements simultaneously at a PRF of 2 kHz and averaged 256 times for the gelatin phantom experiments and 512 times for ex vivo experiments. The ultrasound probe is acoustic-impedance matched to the phantom using coupling gel.

RF-signals corresponding to each of the channels at every scanned point were registered. Data is later processed in a MATLAB (Mathworks, USA) environment in order to generate maximum intensity projection (MIP) images. Three different beamforming strategies were followed to illustrate and quantify the advantages of the dynamic focus beamforming. First, a no-beamforming approach in which, for every scanning point, signals are directly summed up without taking into account the delay between the ultrasound wave and the position of each element of the array, a behaviour analogous to what a single-element plane transducer would present. Second, a fixed focus beamforming strategy where all 128 signals are combined in order to have a fixed focusing position in reception for every scanning point, which imitates a single-element focused transducer placed at a fixed position. Finally, we

evaluate the performance of a DAS beamforming strategy, where the focusing is dynamically repositioned at every measured point to match the location of the laser excitation. For a given scan position, the output signal using the DAS algorithm reads

$$y_{DAS}(t) = \sum_{i=1}^N y_i(t - \Delta_i) \quad (1)$$

where  $N = 128$  is the number of elements of the ultrasound probe,  $y_i(t - \Delta_i)$  is the signal received by the  $i$ th channel of the array considering its corresponding delay  $\Delta_i$ , which is obtained as the three-dimensional distance between the position of the laser focus within the focusing plane F, and the position of the  $i$ th element of the array, assuming a speed of sound  $c = 1540$  m/s.

## 2.4. System configuration for experiments

Four sets of experiments were performed and their results will be presented later in Section 3. First, an initial experiment to determine the lateral resolution of the photoacoustic system using the ESF method, consisting in partially imaging a highly absorbing 180-μm black vinyl strip. Multiple lines were acquired for a total scanned area of  $2 \times 2$  mm<sup>2</sup> for both horizontal and vertical orientations, with step increments of 10 μm. Then, two experiments using polyethylene tubes filled with India Ink, aimed to illustrate the ability to perform large-area images and to evaluate the performance of the different beamforming strategies in terms of SNR. The scanned areas, using step increments of 50 μm in both cases, were nearly 1 cm<sup>2</sup> (1.2 cm × 0.8 cm) and 0.6 cm<sup>2</sup> (2 cm × 0.3 cm), resulting in images having 39862 and 24862 pixels, respectively. Finally, an ex vivo case, imaging a certain portion of the vasculature of a rabbit's ear, in which the scanned area was 0.72 cm<sup>2</sup> (1.2 cm × 0.6 cm), using step increments of 50 μm, resulting in images having 29,282 pixels. All experiments were performed using the same optical power, setting the laser diode driver to half of its maximum range (at 50 V), which means that an optical power of 150 W was eventually delivered to the focal excitation region, as obtained from linear calibration of laser power measurements. This results in a laser pulse energy within the lateral resolution spot area of 5.3 μJ, which means an average fluence of 22.2 mJ/cm<sup>2</sup>. Registered acoustic signals were averaged 256 times for all experiments except for the ex vivo

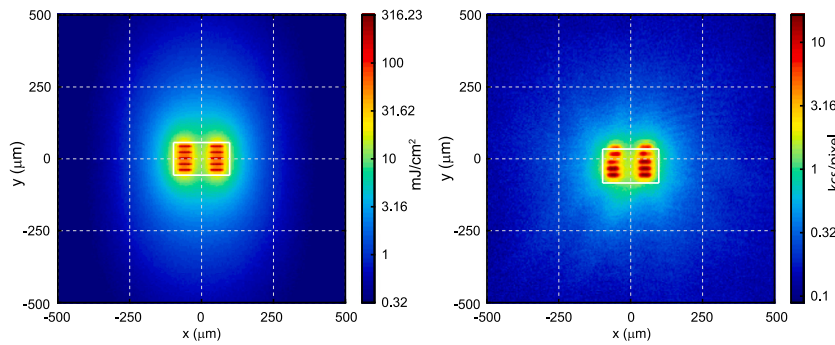


**Fig. 2.** Laser beam spot energy distribution at the focusing plane. (a) Ray-tracing simulation. (b) CCD camera image taken with 60 mm imaging lens and 1:1 magnification. Pixel size in both images is 4.54  $\mu\text{m}$ . White solid line indicates ESF beam spot area.

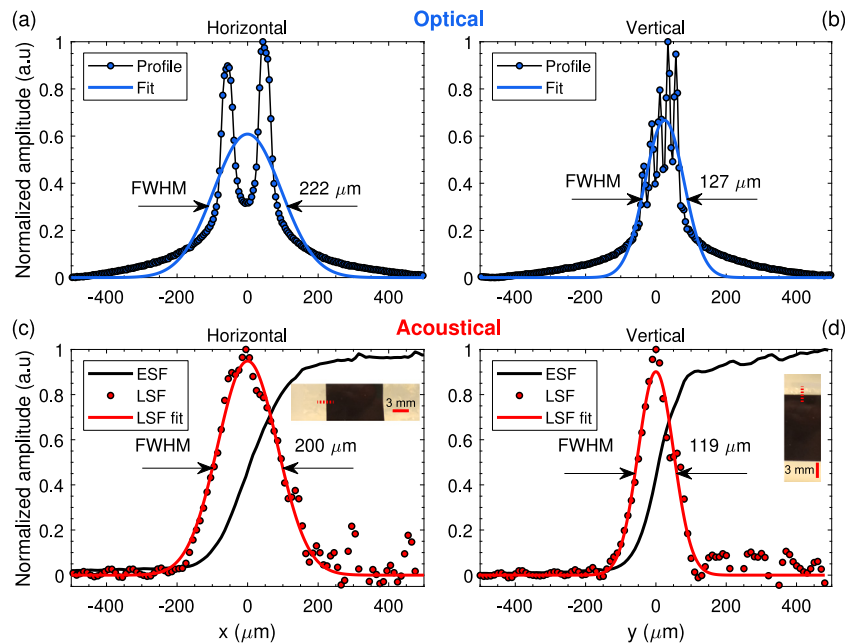


**Fig. 3.** Lateral resolution evaluation. (a) Horizontal and (b) vertical optical image profiles of the laser beam spot at its focus and beam spot size at first order approximation from Gaussian fitting at FWHM. (c) Horizontal and (d) vertical ESFs, LSFs and corresponding Gaussian fittings obtained from photoacoustic measurements.

experiment, where averaging was increased up to 512, since the optical absorption coefficient for blood at the working wavelength is around  $10 \text{ cm}^{-1}$ , more than one order of magnitude lower than for India ink, which is around  $200\text{--}400 \text{ cm}^{-1}$  [1,29].

### 3. Results

#### 3.1. Optical characterization of the laser beam spot

The laser energy distribution at the focusing plane was first reproduced with a Zemax ray-tracing simulation of the optics configuration (Fig. 1), and it was used to estimate the beam energy delivered to a given spot area, by this structured light pattern. Afterwards, the CCD camera image of the beam focal spot shown in Fig. 2(b) was used to get the experimental optical beam spot size from its  $x\text{--}y$  profile projections, as detailed in the next section.

The PLD stack was modelled as an array of 50 single emitters arranged in 2 columns and 5 rows, with 510 W total power emission and 907 nm wavelength, according manufacturer's data and the power measurements of Section 2.1. In this simulation it was also considered the aspheric lenses NIR anti-reflection coatings and mount apertures. Fig. 2(a) shows the simulation output image of the laser beam spot pattern within a  $1 \times 1 \text{ mm}^2$  area at the focusing plane position, which

corresponds to a working distance of 2.3 mm and divergence of around  $22^\circ$  and  $45^\circ$  for horizontal and vertical planes respectively. In order to get the fluence map of the simulated image in  $\text{mJ}/\text{cm}^2$  units, a power calibration was first made by applying the 300.5 W beam power measurement to the sum of all pixels counts within a 6 mm circular area, which corresponds to the input port aperture of the integrating sphere at the focal plane, and hence a total pulse energy of 30.05  $\mu\text{J}$  for a pulse width  $\tau_p = 100 \text{ ns}$ .

In this way, it is obtained a good estimation of the laser pulse energy delivered at the focal plane, which corresponds to 21.7  $\mu\text{J}$  for the simulated 1 mm square area, and 10.7  $\mu\text{J}$  for the laser beam spot area of  $200 \times 119 \mu\text{m}^2$ , as measured by the ESF method described in the following section. A white rectangle is overlaid on Fig. 2 to indicate the laser beam spot area over the fluence distribution.

#### 3.2. Lateral resolution: Edge Spread Function

The lateral resolution of the PAM system, defined by the laser beam spot size, was characterized from both optical and acoustical experimental measurements, as shown in Fig. 3. First, image data from the optical characterization of the laser beam focus of Fig. 2(b), was extracted and averaged for every horizontal and vertical line along the  $x\text{--}y$  image plane rectangular area to obtain the laser beam spot profile

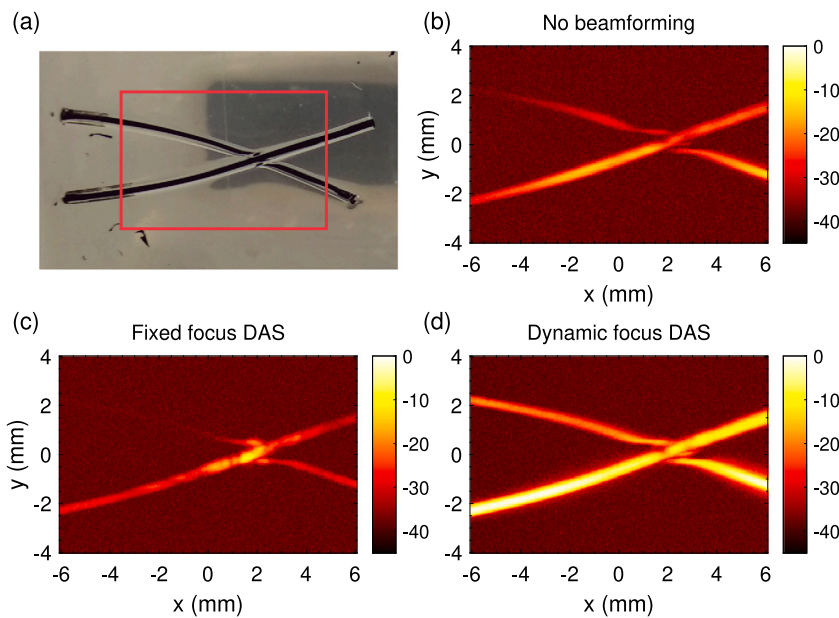


**Fig. 4.** 2D photoacoustic images using gelatin phantoms. (a) Photograph of the surface of the phantom including polyethylene tubes at its surface. The red rectangle represents the scanned area. 2D photoacoustic images of the gelatin phantoms using a single set of experimental data, applying (b) no-beamforming, (c) fixed focus DAS beamforming aimed at the crossing point of the PE tubes and (d) dynamic focus DAS beamforming aiming the focusing point at the focal spot of the laser for every scanned point.

for each orientation, as shown in Figs. 3(a, b). The beam spot size of those profiles are defined by taking the full-width at half-maximum (FWHM) of a Gaussian fit (solid blue lines), as a first order approximation of the more complex line profiles. The resulting measurement of the PLD optical beam excitation spot was  $222 \times 127 \mu\text{m}^2$ . Similar results were obtained for the simulated data, shown in Fig. 2(a), with an estimated spot size of  $217 \times 112 \mu\text{m}^2$ .

For the acoustical characterization, we made use of the edge spread function estimation considering the different horizontal and vertical properties of the PLD beam profile. A highly absorbing 180- $\mu\text{m}$  black vinyl strip was embedded in the phantom at around 1 mm beneath its surface and partially imaged, as shown in the insets of Figs. 3(c, d). The measured photoacoustic profile lines are shown as solid black lines in Figs. 3(c, d) for the horizontal and vertical orientations, respectively. A representative trajectory of the measured profiles is shown in the insets by red dotted lines. All measured profiles within the imaged area were averaged to obtain a single ESF. Their respective spatial derivatives, i.e., linear spread functions (LSF) were fitted using a Gaussian function. The lateral resolution extracted from the FWHM of the fitted curve was 199.8  $\mu\text{m}$  and 118.9  $\mu\text{m}$  for the horizontal and vertical orientations, respectively.

The beam spot sizes measured by optical and acoustical methods show a good agreement between them. This seems to indicate that in the photoacoustic interaction, where the laser energy is converted into a thermoelastic expansion after heating the targeted material, a smoothing of the spikes of the underlying laser distribution is produced, possibly due to the integration of the laser energy density (fluence or intensity) when it is absorbed by the material. Thanks to this observed effect, PLDs with non-uniform patterns can still be used to produce a Gaussian-like photoacoustic beam spots yielding the true lateral resolution as measured by the ESF method.

### 3.3. Gelatin phantoms 2D imaging

To evaluate the performance of the PAM system and graphically show the differences between the different beamforming strategies we first took 2D large-area images of gelatin phantoms including polyethylene tubes filled with India ink (inner diameter 0.42 mm, outer diameter 0.85 mm). Fig. 4(a) illustrates a photograph of the phantom and highlights the imaged area.

Following the acquisition of the RF-signals for all 128 channels of the ultrasound probe at every point of the image, data was processed and summed-up differently according to the three proposed beamforming strategies. First, for the no beamforming strategy, data from every channel were directly summed up (see Fig. 4(b)). Then, for the fixed focus beamforming strategy, time delays for every channel were calculated in order to point the focus in reception at the point (2, 0) mm, and time signals were time-shifted accordingly (Fig. 4(c)). Finally, for the dynamic focus DAS beamforming strategy, the focal law in reception was set to match the location of the imaged pixel using the DAS algorithm, (Fig. 4(d)). Once the beamforming strategy was applied, the photoacoustic image was obtained by considering the MIP, plotting the result in logarithmic scale. These results clearly indicate that if a large-area image is desired, neither the no-beamforming nor the fixed focus beamforming strategies can provide sharp images, failing to achieve enough and uniform contrast for the whole scanned area. On the other hand, when applying a dynamic focus DAS beamforming strategy, the SNR along the imaged area is greatly homogenized and increased around 20 dB, enhancing the overall contrast. Note that the depth of the hollow tubes within the gelatin phantom, with respect to the laser focus, slightly changes along their length resulting in certain intensity variations of the obtained images.

An additional photoacoustic experiment was performed to better quantify the differences between the three beamforming strategies. A single polyethylene tube filled with India Ink was located inside a gelatin phantom nearly at its surface in a quasi-horizontal position, i.e., aligned to the x-axis. Note that since the ultrasound array is a 1D probe, the dynamic focusing strategy is only feasible along the x-axis and z-axis. A photograph of the sample is shown in Fig. 5(a). Photoacoustic images extracted from MIP of the processed time series signals are shown in Figs. 5(b, c, d) for all three beamforming strategies, including the values of gCNR [28] obtained within selected regions of interest (ROI). Finally, Fig. 5(e) represents the comparison of SNR along the horizontal x-axis at the y point corresponding to the centre of the tube.

Results shown in Fig. 5(e) represent a clear picture of the difference in performance between the three beamforming strategies. First, for the sake of consistency, note that the fixed focus and dynamic focus DAS beamforming strategies have the same SNR when evaluated at the focus

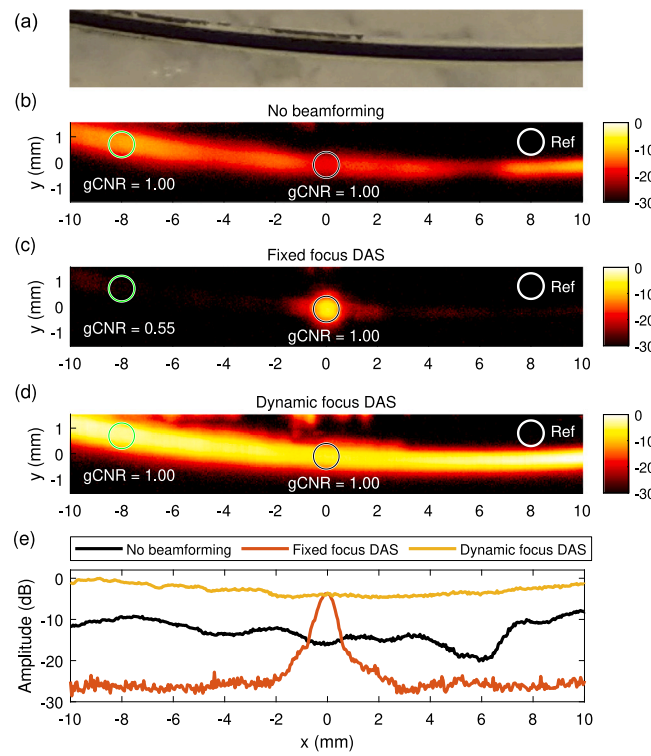


**Fig. 5. SNR comparison between beamforming strategies.** (a) Photograph of the gelatin phantom featuring an India Ink filled PE tube. 2D photoacoustic images using (b) no beamforming, (c) fixed focus beamforming, and (d) dynamic focus DAS beamforming. (e) SNR comparison along the x-axis at the centre of the tube.

position of the fixed focus beamformer. The dynamic focus beamforming strategy offers a quite homogeneous SNR along the polyethylene tube for almost 2 cm, with variations below 3 dB. Moreover, these small variations are influenced by small differences in the depth along the z-axis of the tube, considering its size with respect to the depth of field of the laser at its focus (approximately 1 mm). When comparing these results with a no-beamforming strategy, there exists an overall reduction of 10 to 20 dB in SNR. If compared to the fixed focus beamforming strategy, the SNR increase nearly reaches 30 dB for out-of-focus regions. To further characterize the image quality, gCNR [28] was computed for two ROIs inside relevant target regions (green and black circles) and one inside the reference background (white circle). Results indicate an optimal target visibility for all three beamformers at the centre region (black circle) and a strong reduction of its value for out-of-focus regions when using the fixed focus beamformer.

#### 3.4. Rabbit ear 2D imaging

To evaluate the performance of the proposed PAM system in a more realistic environment, ex vivo images of a rabbit's ear were taken. Rabbit ears were provided by the Instituto de Ciencia Animal (ICTA) of the Universitat Politècnica de València (accredited animal care facility ES462500001091) in agreement with European legislation. Two strategies (no-beamforming and dynamic focus DAS beamforming) were considered for the same set of experimental data. A photograph of the rabbit's ear including a rectangle indicating the scanned area and the corresponding photoacoustic images using the two beamforming techniques are shown in Fig. 6. The obtained results highlight the relevance of the dynamic focus beamforming, shown in Fig. 6(c), not only to homogenize the SNR along the scanned area, but most importantly, in this case, to discern different elements of the rabbit ear's vasculature, which are hardly visible for the no-beamforming case

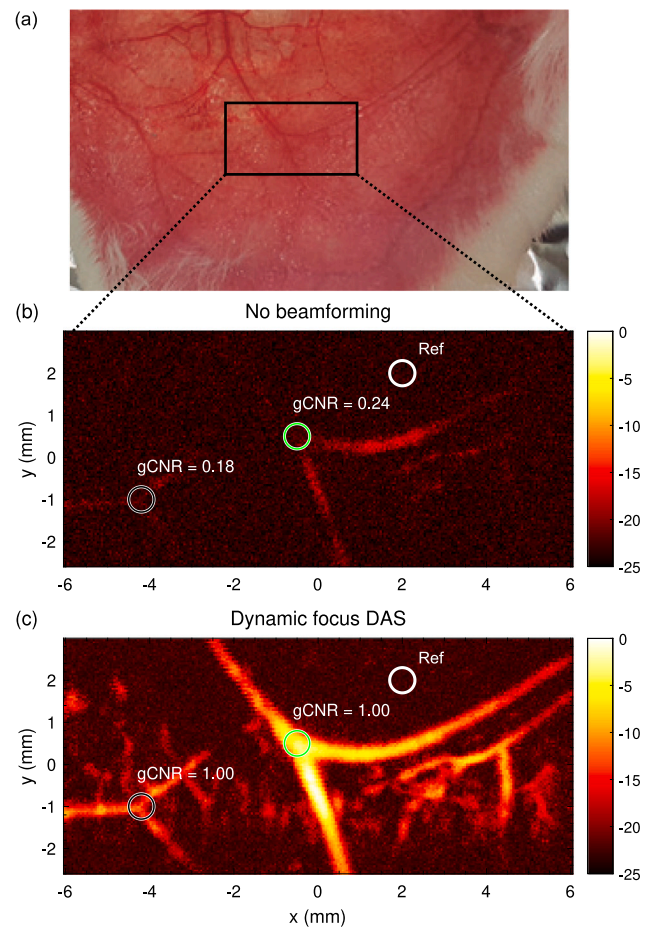


**Fig. 6. Ex vivo rabbit ear 2D PAM imaging.** (a) Photograph of the excised rabbit ear, where the black rectangle indicates the scanned area. PAM images of the rabbit ear vasculature comparing (b) no-beamforming and (c) dynamic focus DAS beamforming.

shown in Fig. 6(b). The obtained gCNR values confirm this statement, as the target visibility is optimal for the two selected ROIs when using the dynamic focus DAS beamformer, while it is strongly reduced for the no-beamforming strategy ( $gCNR = 0.24$ ,  $gCNR = 0.18$ ). The beamformed image highlights the presence of several capillaries of different size and allows to see details that are even hardly visible by a direct visualization of the photograph shown in Fig. 6(a). Note that the SNR improvement obtained in this experiment is consistent with the results presented previously for the phantom, where the improvement was between 10 and 20 dB.

#### 4. Conclusions

In this work, we have compared different detection strategies for array-based low-cost OR-PAM systems, and measured their performance in terms of signal-to-noise ratio and generalized contrast-to-noise ratio. We demonstrated and quantified that DAS beamforming allows to greatly extend the field-of-view of OR-PAM images as compared with unfocused or fixed focus detectors while maintaining image quality. By applying DAS beamforming in OR-PAM systems, the signal-to-noise ratio is increased and spatially homogenized along the imaging plane, with enhanced target visibility as demonstrated by the high values of gCNR obtained using phantoms and ex vivo experiments.

In particular, the laser excitation system was composed of a low-cost PLD controlled by a voltage driver module and two planoconvex aspheric lenses, resulting in a rectangular focal spot of  $200 \times 119 \mu\text{m}^2$  and a pulse energy ranging from 3.2 to 10.7  $\mu\text{J}$ , for a fluence within

the laser focal spot between 13.4 and 45 mJ/cm<sup>2</sup>. The lateral resolution of the system was characterized from both optical and acoustical measurements based on the edge spread function method, obtaining a very good agreement between them.

Images of polyethylene tubes filled with India ink embedded in tissue-mimicking phantoms demonstrated the benefits of applying dynamic focus beamforming in the imaging plane to resolve objects in very large scanning areas (around 1 cm<sup>2</sup> and nearly 40,000 pixels) with an improved and homogenized SNR along the whole imaged area, reaching improvements up to nearly 30 dB compared to a fixed focus configuration. Finally, 1.2-cm wide images of the microvasculature of a rabbit's ear were taken. In this ex vivo experiment capillaries of different sizes were clearly observed all along the image when using the DAS beamformer. The resulting SNR and gCNR values when applying DAS beamforming were similar to those using gelatin phantoms, showing the potential of DAS in OR-PAM systems in a more realistic environment. Note that advanced beamforming algorithms such as DMAS, DS-DMAS, F-DMAS [30–32], sparsity-based beamforming [33], eigen-space based minimum variance [34], short-lag spatial coherence [35], or even synthetic aperture focusing techniques [36,37] could be applied to further enhance SNR in array-based OR-PAM systems.

One of the advantages of DAS beamforming in OR-PAM systems is that the ultrasound probe and the imaged sample can be physically coupled. As there is no need to mechanically align the focus of the detector with the focus of the laser excitation, this strategy allows a fast scan for in vivo imaging of large-area specimens. The total scanning time of OR-PAM images depends on the PRF of the laser, the scanning method, the number of averages and, ultimately, it is limited by the time-of-flight of acoustic waves in soft tissues. Although real-time imaging of large areas might still be difficult to achieve in OR-PAM, imaging large areas within a few minutes is still feasible with the existing technology. In this regard, the imaging speed can be improved dramatically by using higher PRFs combined with fast laser scanning methods such as micro-electro-mechanical systems (MEMS) or galvanometer-based scanning methods. In these configurations, DAS beamforming techniques, as discussed and quantified in this work, can be applied to synchronize the alignment between the optical and acoustical focal spots during large-area scans, improving and homogenizing the signal-to-noise ratio of photoacoustic microscopy images for practical biomedical applications.

## Funding

This research has been supported by the Spanish Ministry of Science, Innovation and Universities through grant "Juan de la Cierva - Incorporación" (IJC2018-037897-I), and program "Proyectos I+D+i 2019, Spain" (PID2019-111436RB-C22), by Programa Operativo Empleo Juvenil, Spain 2014–2020 (MIN19-VAL-13M-004), and by the Agència Valenciana de la Innovació, Spain through grant INNCON00/2020/009. Action co-financed by the European Union through the Programa Operativo del Fondo Europeo de Desarrollo Regional (FEDER) of the Comunitat Valenciana 2014–2020 (IDIFEDER/2018/022). A.C. received financial support from Generalitat Valenciana, Spain and Universitat Politècnica de València, Spain through the grants APOSTD/2018/229 and program PAID-10-19, respectively. A.D. received support from Generalitat Valenciana, Spain through grant GJIDI/2018/A/249.

## CRediT authorship contribution statement

**A. Cebrecos:** Conceptualization, Data curation, Software, Writing - original draft, Writing - review & editing, Supervision. **J.J. García-Garrigós:** Conceptualization, Data curation, Software, Writing - original draft, Writing - review & editing, Supervision. **A. Descals:** Data curation, Software, Writing - review & editing. **N. Jiménez:** Conceptualization, Software, Writing - review & editing, Supervision. **J.M. Benlloch:** Conceptualization, Funding acquisition, Writing - review & editing, Supervision, Project administration. **F. Camarena:** Conceptualization, Funding acquisition, Writing - review & editing, Supervision, Project administration.

## Declaration of competing interest

The authors declare that they have no known competing financial interests or personal relationships that could have appeared to influence the work reported in this paper.

## Acknowledgements

We would like to thank Francisco Marco Jiménez of the ICTA at the Universitat Politècnica de València, who provided the ex vivo samples as well as useful guidance on the handling and proper conservation of the specimens. All authors have read, critically reviewed and agreed to the final version of the manuscript.

## References

- [1] J. Yao, L.V. Wang, Photoacoustic microscopy, *Laser Photonics Rev.* 7 (5) (2013) 758–778.
- [2] S. Jeon, J. Kim, D. Lee, J.W. Baik, C. Kim, Review on practical photoacoustic microscopy, *Photoacoustics* 15 (2019) 100141.
- [3] P. Beard, Biomedical photoacoustic imaging, *Interface Focus* 1 (4) (2011) 602–631.
- [4] K. Maslov, H.F. Zhang, S. Hu, L.V. Wang, Optical-resolution photoacoustic microscopy for in vivo imaging of single capillaries, *Opt. Lett.* 33 (9) (2008) 929–931.
- [5] K. Maslov, G. Stoica, L.V. Wang, In vivo dark-field reflection-mode photoacoustic microscopy, *Opt. Lett.* 30 (6) (2005) 625–627.
- [6] L.V. Wang, J. Yao, A practical guide to photoacoustic tomography in the life sciences, *Nature Methods* 13 (8) (2016) 627.
- [7] C. Zhang, K. Maslov, L.V. Wang, Subwavelength-resolution label-free photoacoustic microscopy of optical absorption in vivo, *Opt. Lett.* 35 (19) (2010) 3195–3197.
- [8] M.-L. Li, J.C. Wang, J.A. Schwartz, K.L. Gill-Sharp, G. Stoica, L.V. Wang, In-vivo photoacoustic microscopy of nanoshell extravasation from solid tumor vasculature, *J. Biomed. Opt.* 14 (1) (2009) 010507.
- [9] H. Zhong, T. Duan, H. Lan, M. Zhou, F. Gao, Review of low-cost photoacoustic sensing and imaging based on laser diode and light-emitting diode, *Sensors* 18 (7) (2018) 2264.
- [10] T.J. Allen, P.C. Beard, Pulsed near-infrared laser diode excitation system for biomedical photoacoustic imaging, *Opt. Lett.* 31 (23) (2006) 3462–3464.
- [11] L. Zeng, G. Liu, D. Yang, X. Ji, Portable optical-resolution photoacoustic microscopy with a pulsed laser diode excitation, *Appl. Phys. Lett.* 102 (5) (2013) 053704.
- [12] T. Wang, S. Nandy, H.S. Salehi, P.D. Kumavor, Q. Zhu, A low-cost photoacoustic microscopy system with a laser diode excitation, *Biomed. Opt. Express* 5 (9) (2014) 3053–3058.
- [13] L. Zeng, G. Liu, D. Yang, X. Ji, Cost-efficient laser-diode-induced optical-resolution photoacoustic microscopy for two-dimensional/three-dimensional biomedical imaging, *J. Biomed. Opt.* 19 (7) (2014) 076017.
- [14] A. Hariri, A. Fatima, N. Mohammadian, S. Mahmoodkalayeh, M.A. Ansari, N. Bely, M.R. Avanaki, Development of low-cost photoacoustic imaging systems using very low-energy pulsed laser diodes, *J. Biomed. Opt.* 22 (7) (2017) 075001.
- [15] M. Erfanzadeh, P.D. Kumavor, Q. Zhu, Laser scanning laser diode photoacoustic microscopy system, *Photoacoustics* 9 (2018) 1–9.
- [16] M.-L. Li, P.-H. Wang, Optical resolution photoacoustic microscopy using a blu-ray dvd pickup head, in: *Photons Plus Ultrasound: Imaging and Sensing* 2014, vol. 8943, Int. Soc. Opt. Photonics, 2014, p. 894315.
- [17] L. Zeng, Z. Piao, S. Huang, W. Jia, Z. Chen, Label-free optical-resolution photoacoustic microscopy of superficial microvasculature using a compact visible laser diode excitation, *Opt. Express* 23 (24) (2015) 31026–31033.
- [18] A. Hariri, J. Lemaster, J. Wang, A.S. Jeevarathinam, D.L. Chao, J.V. Jokerst, The characterization of an economic and portable led-based photoacoustic imaging system to facilitate molecular imaging, *Photoacoustics* 9 (2018) 10–20.
- [19] M. Erfanzadeh, Q. Zhu, Photoacoustic imaging with low-cost sources; a review, *Photoacoustics* 14 (2019) 1–11.
- [20] J. Yao, L.V. Wang, Sensitivity of photoacoustic microscopy, *Photoacoustics* 2 (2) (2014) 87–101.
- [21] T. Allen, E. Zhang, P. Beard, Large-field-of-view laser-scanning or-pam using a fibre optic sensor, in: *Photons Plus Ultrasound: Imaging and Sensing* 2015, vol. 9323, International Society for Optics and Photonics, 2015, p. 93230Z.
- [22] T.J. Allen, O. Ogundade, E. Zhang, P.C. Beard, Large area laser scanning optical resolution photoacoustic microscopy using a fibre optic sensor, *Biomed. Opt. Express* 9 (2) (2018) 650–660.
- [23] L. Song, K.I. Maslov, K.K. Shung, L.V. Wang, Ultrasound-array-based real-time photoacoustic microscopy of human pulsatile dynamics in vivo, *J. Biomed. Opt.* 15 (2) (2010) 021303.

- [24] L. Song, K. Maslov, L.V. Wang, Multifocal optical-resolution photoacoustic microscopy in vivo, *Opt. Lett.* 36 (7) (2011) 1236–1238.
- [25] G. Li, K.I. Maslov, L.V. Wang, Multifocal optical-resolution photoacoustic microscopy in reflection mode, in: *Photons Plus Ultrasound: Imaging and Sensing* 2013, vol. 8581, International Society for Optics and Photonics, 2013, p. 858126.
- [26] P. Hajireza, W. Shi, P. Shao, S. Kerr, R. Zemp, Optical-resolution photoacoustic micro-endoscopy using image-guide fibers and fiber laser technology, in: *Photons Plus Ultrasound: Imaging and Sensing* 2011, vol. 7899, International Society for Optics and Photonics, 2011, p. 78990P.
- [27] F. Zheng, X. Zhang, C.T. Chiu, B.L. Zhou, K.K. Shung, H.F. Zhang, S. Jiao, Laser-scanning photoacoustic microscopy with ultrasonic phased array transducer, *Biomed. Opt. Express* 3 (11) (2012) 2694–2698.
- [28] K.M. Kempski, M.T. Graham, M.R. Gubbi, T. Palmer, M.A.L. Bell, Application of the generalized contrast-to-noise ratio to assess photoacoustic image quality, *Biomed. Opt. Express* 11 (7) (2020) 3684–3698.
- [29] J.R. Cook, R.R. Bouchard, S.Y. Emelianov, Tissue-mimicking phantoms for photoacoustic and ultrasonic imaging, *Biomed. Opt. Express* 2 (11) (2011) 3193–3206.
- [30] J. Park, S. Jeon, J. Meng, L. Song, J.S. Lee, C. Kim, Delay-multiply-and-sum-based synthetic aperture focusing in photoacoustic microscopy, *J. Biomed. Opt.* 21 (3) (2016) 036010.
- [31] M. Mozaffarzadeh, M.H. Varnosfaderani, A. Sharma, M. Pramanik, N. de Jong, M.D. Verweij, Enhanced contrast acoustic-resolution photoacoustic microscopy using double-stage delay-multiply-and-sum beamformer for vasculature imaging, *J. Biophotonics* 12 (11) (2019) e201900133.
- [32] G. Matrone, A. Ramalli, P. Tortoli, G. Magenes, Experimental evaluation of ultrasound higher-order harmonic imaging with filtered-delay multiply and sum (f-dmas) non-linear beamforming, *Ultrasonics* 86 (2018) 59–68.
- [33] R. Paridar, M. Mozaffarzadeh, V. Periyasamy, M. Pramanik, M. Mehrmohammadi, M. Orooji, Sparsity-based beamforming to enhance two-dimensional linear-array photoacoustic tomography, *Ultrasonics* 96 (2019) 55–63.
- [34] S. Shamekhi, V. Periyasamy, M. Pramanik, M. Mehrmohammadi, B.M. Asl, Eigenspace-based minimum variance beamformer combined with sign coherence factor: Application to linear-array photoacoustic imaging, *Ultrasonics* (2020) 106174.
- [35] M.A.L. Bell, X. Guo, H.J. Kang, E. Boctor, Improved contrast in laser-diode-based photoacoustic images with short-lag spatial coherence beamforming, in: *2014 IEEE International Ultrasonics Symposium*, IEEE, 2014, pp. 37–40.
- [36] Z. Deng, X. Yang, H. Gong, Q. Luo, Adaptive synthetic-aperture focusing technique for microvasculature imaging using photoacoustic microscopy, *Opt. Express* 20 (7) (2012) 7555–7563.
- [37] K. Nakahata, K. Karakawa, K. Ogi, K. Mizukami, K. Ohira, M. Maruyama, S. Wada, T. Namita, T. Shiina, Three-dimensional saft imaging for anisotropic materials using photoacoustic microscopy, *Ultrasonics* 98 (2019) 82–87.